

1 **Analysis of spatial transcriptomics at varying resolution levels using the unified**
2 **framework of SpaSEG**

3 Yong Bai^{1,*†}, Xiangyu Guo^{1,†}, Keyin Liu^{1,2,†}, Qihong Luo¹, Yingyue Wang^{1,3}, Jianhua
4 Yin¹, Yuxiang Li¹, Ao Chen^{1,4}, Xun Xu^{1,5}, Xin Jin^{1,*}

5

6 ¹BGI-Shenzhen, Shenzhen, 518083, Guangdong, China

7 ²Department of Biomedical Engineering, Southern University of Science and
8 Technology, Shenzhen, 518055, China

9 ³School of Life Sciences, Southern University of Science and Technology, Shenzhen
10 Guangdong, 518055, China

11 ⁴Department of Biology, University of Copenhagen, Copenhagen 2200, Denmark

12 ⁵Guangdong Provincial Key Laboratory of Genome Read and Write, Shenzhen 518120,
13 China

14 *Correspondence email: baiyong@genomics.cn, jinxin@genomics.cn

15 †These authors contributed equally to this work: Yong Bai, Xiangyu Guo, Keyin Liu.

16

17 **Abstract**

18 Recent improvements in spatial transcriptomics technologies have enabled the
19 characterization of complex cellular mechanisms within tissue context through
20 unbiased profiling of genome-wide transcriptomes in conjunction with spatial

21 coordinates. These technologies require a systematic analysis approach to deciphering
22 the complex tissue architecture. Here, we develop SpaSEG, an unsupervised
23 convolutional neural network-based method towards this end by jointly learning gene
24 expression similarity of spots and their spatial contiguity via adopting a loss
25 function for spatial boundary continuity. Using several spatial transcriptomics datasets
26 generated by different platforms with varying resolutions and assayed tissue sizes, we
27 extensively demonstrate that not only can SpaSEG better identify spatial domains, but
28 also be much more computationally and memory efficient than existing methods. In
29 addition, SpaSEG is able to effectively detect genes with spatial expression patterns
30 and infer spot-wise intercellular interactions as well as cell-type colocalization within
31 the tissue section by utilizing the identified domains. Taken together, our results have
32 indicated the flexibility of SpaSEG in multiple analysis tasks in spatial transcriptomics,
33 making it as a desirable tool in facilitating the exploration of tissue architecture and the
34 knowledge of underlying biology.

35 **Introduction**

36 Coordinated activities of diverse cells with the spatial context in tissues that underlie
37 their communications with surroundings and sophisticated biological processes can be
38 characterized by spatial gene expression patterns. Emerging spatial transcriptomics (ST)
39 technology has allowed the unbiased profiling of genome-wide gene expressions with
40 physical capture sites (referred to as spots), offering a quantitative and spatial snapshot
41 of cellular heterogeneity across a tissue section [1-3]. Recent years have witnessed
42 considerable progress in the ST experimental methods including the imaging-based *in-*
43 *situ* transcriptomics approaches like MERFISH [4] and seqFISH[5], and the next-
44 generation sequencing (NGS)-based approaches such as Slide-seqV2 [6], 10x

45 Genomics Visium [7], and Stereo-seq [8]. These methods have reached an astonishing
46 resolution from multicellular to single-cell or even subcellular level with varying gene
47 throughput, delivering unprecedented insights into tissue-specific function,
48 development, and pathology through elucidating tissue architectures with myriad cell
49 types [9, 10].

50 A pivotal task in ST data analysis is to identify spatial domains defined as regions in
51 the tissue section with coherence in both gene expressions and spatial dependency. The
52 identification of spatial domains serves unravelling tissue structures, facilitating the
53 characterization of cell type composition and transcriptomic profiles in the tissue
54 microenvironments [8, 11, 12]. Conventional approaches to arrange spots into distinct
55 spatial domains resort to clustering methods such as Leiden [13] that only take into
56 account gene expressions without considering localization information, usually leading
57 to the loss of spatial contiguity. Recently, several deep learning-based and
58 statistical based methods have been developed to enhance spatial domain identification
59 through incorporating gene expression with spatial information, including SEDR [14],
60 BayesSpace [15], SpaGCN [16], stLearn [17] and Giotto [18], to name a few. Despite
61 promising performance, these methods are only applied on the ST datasets with limited
62 spots and thereby may be fragile for larger tissue section with higher capture resolution.
63 Besides, these methods performing spatial clustering is absent of considering the
64 boundary constraint of spatial domains.

65 Additionally, knowledge of biological functions associated with spatial domains
66 necessitates pinpointing genes that exhibit spatial expression variations and patterns
67 known as spatially variable genes (SVGs). A handful of methods such as trendsceek
68 [19], SpatialDE[20] and SPARK[21] have been proposed to identify SVGs by modeling

69 spatial dependency of gene expressions and conducting correlation testing between the
70 distribution of gene expression and spatial localization. These methods apparently
71 neglected spatial domains and may obtain suspectable spatial gene expression patterns,
72 failing to fully reflect tissue-specific spatial functions. Moreover, spatial variations in
73 gene expression across spatial domains can imply spatial patterns in cell-cell
74 interactions (CCIs) in a tissue [22]. However, the majority of existing methods do not
75 present the automatic detection of CCIs across whole tissue section using ST data.

76 Here, we propose SpaSEG, a simply yet powerful unsupervised convolutional neural
77 network (CNN)-based model to jointly identify spatial domains, SVGs and CCIs. In
78 brief, SpaSEG first establishes an unsupervised CNN network through learning gene
79 expression similarity in conjunction with spatial coordinates to detect spatial domains.
80 SVGs are then detected for each spatial domain to ensure spatial gene expression
81 patterns. CCIs are further examined by investigating enriched expression of ligand-
82 receptor (L-R) pairs in both intra and inter spatial domains. By analyzing several
83 datasets that encompass a wide range of ST platforms, including 10x Genomics Visium,
84 Slide-seqV2, seqFISH, MERFISH, and Stereo-seq, we extensively demonstrate that
85 SpaSEG exhibits superior performance on the identification of spatial domain over the
86 existing state-of-the-art methods. We also use ST datasets of mouse embryo to examine
87 the detection of SVGs, as well as mouse brain and human breast cancer section to
88 delineate L-R pairs in normal and tumor microenvironment, respectively. Through
89 comprehensive analyses, we show that SpaSEG is computational and memory efficient
90 as well as applicable for diverse ST platforms and analysis tasks, serving as a desirable
91 tool to explore tissue architecture and cellular characterization for different size of
92 tissue section at varying resolutions.

93 **Results**

94 **Overview of SpaSEG**

95 SpaSEG starts with raw spatial transcriptomic data preprocessing through low-quality
96 genes and poor spots removal, gene measure normalization and log-transformation, as
97 well as principal component analysis (PCA) and z -score scaling, leading to a d -
98 dimensional feature vector $\mathbf{s}_n \in \mathbb{R}^d$ for each spot n (Fig. 1a). SpaSEG then converts
99 the low-dimensional representation of spots with spatial coordinates to an image-like
100 tensor, where spots are analogous to image pixels while the corresponding d -
101 dimensional feature vectors to image channels. Accordingly, the spatial domain
102 identification problem can be regarded as the pixel-wise image segmentation problem
103 in an unsupervised fashion.

104 SpaSEG responsible for spatial domain identification is a CNN-based network model
105 that consists of a batch normalization layer, two stacking convolutional modules and a
106 refinement module (Fig.1b). The network model yields a response representation $\mathbf{y}_i \in$
107 \mathbb{R}^d for each spot i . To initialize model parameters, we first pre-train the model using
108 the mean squared error (MSE) loss between \mathbf{s}_n and \mathbf{y}_n for all spots. Then, the
109 softmax likelihood \mathbf{p}_n and the related pseudo-label c_n for each spot n can be
110 obtained, and thus the classic cross entropy loss \mathcal{L}_{seg} is applied in the subsequent
111 training iterations. To encourage continuity of neighboring spots, we additionally
112 calculate L1-norm of boundary gradients for each spot with its spatial location as
113 domain boundary constraint loss \mathcal{L}_{spa} , inspired by the previous study [23]. To this end,
114 we optimize the joint loss of the weighted sum of \mathcal{L}_{seg} and \mathcal{L}_{spa} for progressively
115 enhancing spot classification during iterative learning while preserving spatial

116 dependency and continuity (Supplementary Figure 1). Finally, spots that present similar
117 gene expression and spatially continuous coordinates are clustered into the same
118 domain, and the detection of SVGs and CCIs based on the identified domains are further
119 investigated (Fig. 1c). We also showcase the capability of SpaSEG to integrated analysis
120 of multiple tissue sections, thus helping to discover spatial domains in different tissue
121 samples.

122 **SpaSEG improves spatial domain identification on the human dorsolateral** 123 **prefrontal cortex dataset**

124 To evaluate the performance of SpaSEG on spatial domain identification, we first
125 downloaded the publicly available dataset of the 10x Genomics Visium human
126 dorsolateral prefrontal cortex (DLPFC) [12] and used as a benchmark. This manually
127 annotated dataset is composed of 12 sections that cover six neuron layers and white
128 matter with the number of spots ranging from 3460 to 4789 (Supplementary Table 1).
129 To compare with SpaSEG, we chose a commonly used non-spatial clustering method
130 Leiden plus five recently published state-of-the-art methods, including stLearn, Giotto,
131 SpaGCN, BayesSpace, and SEDR. Apart from qualitative visualization analysis, two
132 widely used evaluation metrics of adjusted rand index (ARI) [24] and normalized
133 mutual information (NMI) [25] were employed to quantitatively assess performance of
134 these methods.

135 SpaSEG outperformed the competitive methods for the identification of spatial domains
136 on the 12 DLPFC sections in terms of its highest values of ARI (0.532 ± 0.058 ; mean
137 \pm s.d.) and NMI (0.644 ± 0.020) (Fig. 2a and Supplementary Table 3,4) while requiring
138 the least running time and memory usage except for Leiden partially due to its lack of
139 leveraging spatial information during clustering (Supplementary Figure 2,

140 Supplementary Table 5, 6). SpaSEG also yielded the neatest spatial domains with
141 clear boundaries to depict the tissue structures of all 12 sections in the comparison of
142 other methods (Supplementary Figure 3). As a representative example of section
143 151673 (Fig. 2b), we observed that spatial domains unraveled by SpaSEG (ARI=0.554)
144 had the best consistency with the manual annotations in spite of failure to detect the
145 thinnest layer 4 separately (Fig.2c). Interestingly, this failure also took place in all other
146 methods, plausibly because of the small number of spots in the layer 4 that may have
147 gene expressions similar to the adjacent layer. All methods struggled discerning layers
148 4 and 5. Although being able to obtain comparable clustering accuracies and promising
149 layer structures, SpaGCN (ARI=0.457) and BayesSpace (ARI=0.546) appeared to
150 improperly separate the white matter into two domains with ragged boundaries, while
151 SEDR (ARI=0.522) incorrectly merged the layers 4, 5 and 6 into a single layer. The
152 spatial domains detected by Leiden, stLearn and Giotto massively mixed many
153 unexpected outliers, leading to the rough tissue structures and the poorest clustering
154 ARI values of 0.335, 0.306 and 0.291, respectively.

155 **SpaSEG displays high robustness on diverse ST platform datasets and high**
156 **scalability on large tissue section with high resolution**

157 Next, we sought to test whether SpaSEG was robust to identify spatial domains on the
158 datasets generated by different ST platforms such as Slide-seqV2, Stereo-seq,
159 MERFISH, and seqFISH. Considering the above results regarding clustering accuracy
160 and concordance of identified spatial domains with manual annotations, we only
161 compared SpaSEG with SpaGCN and BayesSpace, as well as Leiden serving as a
162 baseline method in the following experiments.

163 We first applied SpaSEG on the mouse hemibrain Stereo-seq data [8]. This image-based

164 cell segmentation dataset has 50140 segmented cells (i.e., spots) and 25879 genes. As
165 expected, SpaSEG can well uncover spatial regions of mouse hemibrain in comparison
166 with Leiden and SpaGCN (Fig. 3a). BayesSpace did not successfully perform spatial
167 clustering on this dataset because of the excessive large number of spots. Moreover, the
168 LISI values displayed that SpaSEG reached significant more accuracy than Leiden
169 ($p < 2.2e-16$, Mann-Whitney U test) except for SpaGCN (Fig.3d). However, SpaSEG
170 can clearer outline many cell-type spatial localizations than SpaGCN (Fig.3a),
171 including neuroprotective astrocyte 2 types in thalamus, granule cells of dentate gyrus
172 (GN DG), excitatory glutamatergic neurons from CA1 (EX CA1), and excitatory
173 glutamatergic neurons from CA3 (EX CA3).

174 Then, we examined the scalability and efficiency of SpaSEG on large tissue section
175 with high resolution. To achieve this, we analyzed an unreported whole adult mouse
176 brain spatial transcriptomic data generated by Stereo-seq [8]. To facilitate our analysis
177 at different resolution levels, we aggregated transcripts of the same gene into non-
178 overlapping bin areas that covered corresponding DNB spots. These bins were of sizes
179 in 10 μm diameter (bin20; 20 \times 20 DNB sites; equivalent to \sim 1 medium mammal cell
180 size), 25 μm diameter (bin50; 50 \times 50 DNB sites), 50 μm diameter (bin100; 100 \times 100
181 DNB sites), and 100 μm diameter (bin200; 200 \times 200 DNB sites). As a result, we
182 obtained four binned Stereo-seq ST datasets with the number of bins from 5420 to
183 526716 (Supplementary Table 7). The annotation of whole mouse brain from Allen
184 Reference Atlas [26] is used as the reference and we choose resolution bin50 as a
185 representative in our study. SpaSEG can well characterize the structures of the whole
186 adult mouse brain such as cortex layers and hippocampus (including DG-sp, CA3sp or
187 CA1sp subfields) at all four resolution levels (Fig.3b, Supplement Figure 4). In contrast,
188 Leiden mixed the domains with other spots at bin20 and bin50 resolution levels, neither

189 uncovering clear cortex layers at bin100 resolution nor separating DG-sp and CA3sp at
190 bin200. SpaGCN was not able to handle Stereo-seq data at bin20 resolution due to the
191 substantial number of bins (526716) and running out of memory. Neither it yielded
192 continuous and neat spatial domains nor uncover DG-sp and CA3sp separately at
193 resolution levels of bin50, bin100, and bin200. BayesSpace cannot successfully
194 perform spatial domain identification for Stereo-seq data at high resolution levels of
195 bin20, bin50, and bin100 because of large number of bins. The LISI values of resolution
196 bin 50 demonstrated that SpaSEG identifying spatial domain was significant more
197 accurate than Leiden, SpaGCN ($p < 2.2e-16$, Mann-Whitney U test; Fig.3d). Moreover,
198 SpaSEG took 12.1 minutes to perform spatial domain identification for the bin20 data
199 (2.5 times faster than Leiden) while 4.2 minutes with only 3.5G memory for the bin50
200 data, 26 times extraordinary faster and 35 times fewer memory usage than SpaGCN
201 that suffered from considerable computational burden and took 110 minutes and 122.4G
202 memory (Supplementary Table 7).

203 We next used the mouse hippocampus Slide-seqV2 data with 53208 spots and 23264
204 genes at 10 μm diameter resolution that can capture gene expressions at cellular level
205 [6] (Supplementary Table 8). The annotation of hippocampus structures from the Allen
206 Reference Atlas was employed as reference [26] (Fig. 3c). As expected, SpaSEG can
207 better outline the topology of the tissue based on the identified neat spatial domains and
208 sharp boundaries than that of Leiden, SpaGCN and BayesSpace (Fig.3c). For example,
209 in addition to different cortical layers, SpaSEG was also able to clearly delineate the
210 pyramidal layer of Ammon's horn and the granule cell layer of the dentate gyrus. More
211 specifically, SpaSEG successfully depicted subfields of Ammon's horn such as CA1
212 (CA1so, CA1sp, and CA1sr) and CA3 (CA3so, CA3sp, and CA3sr), as well as subfields
213 of dentate gyrus including DG-mo, DG-sg, and DG-po. Spatial domains for CA2 were

214 not uncovered separately partly due to the few spots with gene expression similar to
215 nearby domains. Owing to the lack of manual annotation on this dataset, we calculated
216 the local inverse Simpson's index (LISI) to measure the clustering performance. As a
217 result, SpaSEG reached a significantly lower LISI value than other three methods
218 ($p < 2.2e-16$, Mann-Whitney U test; Fig 2d), suggesting its highest accuracy for spatial
219 domains detection with high resolution data.

220 We then utilized the mouse hypothalamic preoptic region data generated by MERFISH
221 [4]. This annotated dataset contains 4975 single cells (i.e., spots) and 160 genes.
222 SpaSEG achieved the ARI value of 0.46, which was higher than all other methods of
223 Leiden (0.38), SpaGCN (0.26) and BayesSpace (0.33) (Fig. 2e. Moreover, SpaSEG also
224 can delineate the spatial distribution of cell classes with spatial dependency such as
225 ependymal, inhibitory, excitatory, mature OD, and mural, which were agreement to the
226 annotations. We further employed the mouse organogenesis seqFISH data [5]. This
227 dataset consists of 19416 single cells and 351 genes with a total of 22 cell types
228 annotated. Compared to Leiden, SpaGCN and BayesSpace, SpaSEG yielded the highest
229 ARI value of 0.46 (Fig. 2f). SpaSEG can better depict the spatial distribution of cell
230 classes than other method, including three germ layers of ectoderm, mesoderm and
231 endoderm, which were in consistent with the original study and known anatomy [27].
232 These results demonstrated that SpaSEG had the high accuracy for spatially clustering
233 imaging-based *in-situ* transcriptomic data.

234 **SpaSEG can successfully detect spatially variable genes (SVGs)**

235 Next, we applied SpaSEG to detect SVGs for the validation of the identified spatial
236 domain. Similar to previous study [16], we first examined the detected SVGs for each
237 domain in the DLPFC section 151673 originally with 3639 spots and 33538 genes.

238 SpaSEG finally detected 143 SVGs with low false discovery rate (FDR)-adjusted P
239 values (<0.05), of which 126 genes were specifically expressed highly in domain 0,
240 while the rest 17 genes were in the remaining domains (Supplementary Table 10). The
241 Gene Ontology (GO) term enrichment analysis indicated the most SVGs enriched in
242 domain 0 were significant related to white matter such as central nervous system
243 myelination, neural myelin sheath, and structural constituent of myelin sheath
244 (Supplementary Figure 5d). SpaSEG detected single representative genes for each of
245 neuronal layers and white matter. For example, *PLP1*, *CNP*, *GFAP*, *CRYAB*, *TF*, *MOBP*
246 gene was enriched in domain 0 (white matter), *CAMK2N1*, *ENC1*, *HPCAL1*, *HOPX* in
247 domain 2(layer2, 3), *NEFL*, *NEFM*, *SNCG* in domain 3(layer 3), *PCP4*, *TMSB10*,
248 *TUBB2A* in domain 4(layer 4, 5) and *MALAT1* was in domain 6(layer 1) (Fig.4a, b,
249 Supplementary Figure 5a). By contrast, SpaGCN detected only 67 SVGs while
250 SpatialDE and SPARK can totally detect 3661 and 3187 SVGs, respectively
251 (Supplementary Figure 5c). However, SVGs detected by SpatialDE and SPARK did not
252 necessarily show domain specificity. The Moran's I values and Geary's C values for
253 SVGs detected by SpaSEG were significantly lower than that detected by SpatialDE
254 ($p < 2.2e-16$, Mann-Whitney U test) and SPARK ($p < 2.2e-16$, Mann-Whitney U test) but
255 showed no significant difference against that detected by SpaGCN ($p = 0.07, 0.01$
256 Supplementary Figure 5b). These results suggested that SpaSEG can detected more
257 domain-specific SVGs than SpaGCN, SpatialDE and SPARK while maintained the
258 similar accuracy against SpaGCN in spite of being slightly inferior to SpaGCN in terms
259 of the Moran's I value and Geary's C value. These results demonstrated that SpaSEG
260 outperforms SpaGCN in identifying spatial patterns for genes.

261 Then, we applied SpaSEG to detect SVGs on the unannotated mouse embryo Stereo-
262 seq data with 72944 spots (bin50, 25 μm diameter per spot) and 28879 genes. Based

263 on the 30 identified spatial domains (Fig.4c), SpaSEG detected a total of 490 SVGs that
264 was more than SpaGCN (n=458) (mean of Moran's I for SpaSEG 0.361 and mean of
265 Geary's C = 0.616, Fig.4d, e). These results demonstrated that SpaSEG outperforms
266 SpaGCN in identifying spatial patterns for genes. Of particular interest in the following
267 analyses were domain 1 (brain), domain 4 (epidermis), and domain 7 (cartilage
268 primordium/bone), which were associated with 178 SVGs, 18 SVGs, and 18 SVGs
269 respectively (Supplementary Table 11-13). These SVGs showed transcriptionally
270 distinct patterns that distinguished the three spatial domains (Fig.4h). We further select
271 top 5 genes that were highly expressed for each domain. For example, top 5 SVGs
272 highly expressed in domain 1 contains brain development associated genes of *Nnat*,
273 *Tuba1a*, *Mapt*, and brain marker genes *Stmn2*, *Tubb2a*, and top 5 SVGs in domain 4 of
274 *Krt10*, *Krt15*, *Krt77*, *Lor*, *Krtdap*, and top 5 SVGs in domain 7 of *lbsp*, *Coll1a1*, *Coll1a2*,
275 *Sparc*, *Serpinh1* (Fig.4f). We also depicted spatial expression for each of top 2 SVGs
276 that demonstrate strong spatial patterns in corresponding spatial domain (Fig.4g). GO
277 enrichment analysis of the SVGs showed that a total 457 GO terms and 40 Kyoto
278 Encyclopedia of Genes and Genomes (KEGG) pathways were enriched in cluster 1
279 (brain), of which many of these GO terms and KEGG paths are associated with the
280 development of the nervous system (Fig.4i), for example, growth cone (GO 0030426),
281 site of polarized growth (GO 0030427), distal axon (GO 0150034). In cluster 4
282 (epidermis), 18 SVGs are selected (q value < 0.05 and p value < 0.05) for the
283 enrichment analysis, a total 72 GO terms and 11 KEGG pathways were enriched and
284 most of these GO terms and KEGG pathways are related to keratin and epidermal cells,
285 (Fig.4i) such as intermediate filament (GO 0005882), intermediate filament
286 cytoskeleton (GO 0045111), keratin filament (GO 0045095). While in cluster 7
287 (cartilage primordium/bone), the most significant GO terms and KEGG paths are

288 related to collagen and cartilage or bone development (Fig.4i), collagen-containing
289 extracellular matrix (GO 0062023), fibrillar collagen trimer (GO 0005583), banded
290 collagen fibril (GO 0098643). In addition, SpaSEG is also capable to identified fine
291 structure of mouse embryos and we further analysis the spatial variable genes in toes.
292 Several representative marker genes are identified (Fig.4j), such as *Krt10* (skin tissue),
293 *Dcn* (connective tissue), *Col2a1* (cartilage primordium). These results demonstrate that
294 SpaSEG could effectively and accurately identify spatial variable based on our spatial
295 segmentation results.

296

297 **SpaSEG facilitates the investigation of ligand-receptor interactions**

298 Most of cell-cell interactions and crosstalks are mediated by ligand-receptor (LR)
299 interactions [ref]. To facilitate the exploration of putative intercellular interaction across
300 the entire tissue section, we proposed a method to conduct LR interaction analysis by
301 leveraging the spatial domains identified by SpaSEG and the co-expressions of the
302 ligands and receptors. Here we applied the LR interaction analysis on the adult mouse
303 brain Stereo-seq data at bin200 resolution with spatial domains identified by SpaSEG
304 (Fig.5a). In order to further validate the accuracy of our clustering result, we first
305 analyzed the SVGs in cortex (Fig.5d) and found that *Lamp5*, *Nrgn* are specifically
306 enriched in cluster 5 (cortex layer 2/3), *Pvalb* gene in cluster 16 (cortex layer 4 or 5)
307 and *Tbr1* in cluster 7 (cortex layer 5/6). Region specific SVGs are also found in
308 hippocampus (Fig.5e), such as *Tmem54*, *Pantr1* in cluster 4 (CA1/2), *Hpca* and *Ddn* in
309 cluster 17 (CA3) and *Wipf3* in cluster 11 (DG). A total of 267 significant ligand-receptor
310 pairs are first identified by CellPhoneDB (Supplementary Table 14), of which a large
311 number of LR interactions are enriched in cortex area as showed in the overall LR score

312 heatmap (Fig.5b). The cell types are annotated by cell2location according to the max
313 confidential spot-level cell type deconvolution score and we observed that the
314 deconvolution result could well depict the analogy of the adult mouse brain (Fig. 5c).
315 Then we calculated the Spearman correlations between spot-wise cell type
316 deconvolution scores with its corresponding LR scores, in which a positive correlation
317 suggests as the colocalization of LR pairs with specific cell types. We found a majority
318 of cell types between cortex, hippocampus and amygdala displayed highly positive
319 correlations, including cell types of Astrocytes and Excitatory neuros that suggested
320 their well colocalization in spatial context of the tissue (Fig. 5f). For example, the ligand
321 Il34 (Interleukin-34) and receptor Csf1r are highly active in the cortex, hippocampus
322 and amygdala (cluster 5,7,8,9,10,12,16), which corresponding to the conclusion that
323 Il34 identified as a tissue-specific ligand of Csf-1 receptor (Csf1r) is mainly expressed
324 in brain cerebral cortex (Fig. 5f, g). Our result also shows that Cholecystokinin (Cck)
325 and its receptor Cckbr are enriched in cortex, hippocampus, amygdala and piriform
326 cortex [28]. Meanwhile, we find that Bdnf_Sort1 and Bdnf_Ntrk2 are enriched in cortex
327 and hippocampus [29], which may be related to increased or decreased volume of the
328 hippocampus.

329 **SpaSEG enables to elucidate the ligand-receptor interactions in Invasive ductal** 330 **carcinoma**

331 To further validate our LR interaction results identified by SpaSEG, we analyzed a
332 breast cancer sample originally published in BayesSpace [15] with tumor regions being
333 annotated by the pathologist (Fig. 6a). The sample was an estrogen receptor-positive
334 (ER⁺), progesterone receptor-negative (PR⁻), human epidermal growth factor receptor
335 (HER)2-amplified (HER2⁺) invasive ductal carcinoma (IDC). The dataset was

336 generated by 10x Genomics Visium, leading to a total of 4727 spots in tissue and 36601
337 genes with a median of 2964 genes per spot. To allow cell2location for cell type
338 mapping at spot level, we downloaded a published breast cancer scRNA-seq dataset as
339 the reference that comprised 16 primary tumors [30] (11 ER⁺ and 5 HER2⁺) with cell
340 types being annotated.

341 Spatial clusters obtained by applying SpaSEG were able to accurately distinguish
342 regions among invasive carcinoma (cluster 0, 2,3, 8 and 9), carcinoma in situ (cluster
343 6), and benign hyperplasia (cluster 2) as well as non-tumor tissue (cluster 1,5 and 7),
344 which were strong accordance with histopathological annotations (Fig. 6b). Cell types
345 mapping using cell2location showed that, compared to other clusters, predominant
346 proportions of cancer cells resided at invasive tumor regions (cluster 0, 2,3, 8 and 9)
347 while non-tumor regions (cluster 1,5 and 7) were enriched for more immune-related
348 cells than other regions such as B cells, cancers associated fibroblasts (CAFs), T cells,
349 and plasmablasts (Fig. 6d and 6f). These findings indicated that SpaSEG can well
350 capture the inter- and intra-tumor heterogeneities at molecular level. Spatially co-
351 expressed LR pairs and its corresponding potential interaction cell types are showed in
352 Figure 6e. By conducting cell-cell interaction analysis, we observed many interactions
353 around the immune-invasive areas, especially between cluster 5 and cluster 0,4,3,9
354 (Fig.6c), and found colocalizations of cell types such as B cells and T cells,
355 macrophages and T cells, CAFs and T cells (Fig. 6e) For example, ligand PTPRC
356 secreted by T cells is an essential regulator in mediating T- and B-cell antigen
357 processing by targeting the CD22 receptor in B cells [31, 32], playing a major role in
358 adaptive immune response. T cells communicated with dendritic cells (DCs) through
359 ligand PTPRC and receptor MRC1 [32, 33] (Fig. 6g, h). The mannose receptor (MRC1)
360 expressed on DCs acts as a direct regulator of CD8⁺ T-cell activity by interacting with

361 CD45[34, 35], which will result in the up-regulation of cytotoxic T-lymphocyte-
362 associated Protein 4 (CTLA-4) and the induction of T-cell tolerance. The cytokine
363 macrophage migration inhibitory factor (MIF) which constitutively found in
364 macrophage sustains pro-inflammatory function and cell proliferation. And its receptor
365 CD74 is also found in T-cells as previous literatures indicates and MIF_CD74 (Fig. 6g,
366 h) shows significant high Spearman correlation with T cells in our study. In addition,
367 we also detected that Galectin-9 (LGALS9 secreted by macrophages, monocytes)
368 served as a ligand for immune checkpoints HAVCR2[30, 36, 37] (Fig. 6 e, g, h) (highly
369 correlated with NKT cells, CD4+, CD8 T cells) and contributes to anti-cancer immune
370 suppression by killing cytotoxic T lymphocytes and impairing the activity of natural
371 killer (NK) cells[38], which is a promising target for immunotherapy. Apart from the
372 active immune cell-cell interaction in TME, crosstalk between stromal cells and
373 immune cells is also of great importance for angiogenesis, tumor invasion and
374 metastasis. We detected that CAF ligand CXCL12 and its cognate T cell receptor
375 (CXCR4/CXCR3) (Fig. 6g, h) are among the top ranked cell types for CXCL12_
376 CXCR4/CXCR3 pairs [39, 40], of which the CAF mainly promotes tumor growth by
377 the secretion of SDF-1. Besides, CAF associated LR pairs like TIMP1_FGFR2,
378 C3_C3AR1 [41, 42] (Fig. 6g, h) could also be observed. And the endothelial cells
379 derived gene VEGFB, PDGFB, ACKR1 that could induce new blood vessel formation
380 and stimulate cell proliferation and migration via interaction with NRP1 [43], LRP1
381 and the chemokine ligand CCL5.

382 Therefore, it is significant to understand the cell-cell interactions between macrophages
383 and other immune cells and the factors that enhance existing anticancer treatments.
384 These results proved that SpaSEG could be served as a handful tool for LR analysis in
385 pathology, suggesting potential patterns of most likely cell-cell interactions.

386 **Discussion**

387 Identification of spatial domain is a significant process in spatial transcriptomic data
388 analyses. SpaSEG harmoniously integrated gene expression information and spatial
389 coordinates into one three-dimensional matrix as model input. Through feeding the
390 input data to the convolutional neural network, SpaSEG learns the gene expression
391 similarity and spatial contiguity simultaneously with the optimization of the gene
392 expression similarity loss and the spatial continuity loss and ultimately identifies
393 separate spatial domains. In our study, we firstly demonstrate its strong ability in
394 differentiating distinct layers and superior performance relative to existing alternatives
395 in DLPFC benchmarking dataset. To further validate the utility of SpaSEG in ST data
396 of diverse resolutions, we artificially simulated four datasets representing different
397 levels of resolution by utilizing the adult mouse brain data generated by Stereo-seq,
398 SpaSEG could uniformly profile significant functional regions, such as Cerebral Cortex
399 layers (CTX), Thalamus (TH), Hypothalamus (HY) and HPF (hippocampal formation
400 areas) [44]. Although SEDR also performed clustering analysis on mouse olfactory bulb
401 data from Stereo-seq and exhibited its efficacy to handle high resolution data, it suffers
402 from high computational burden in constructing graphs for such high throughput and
403 high-resolution spatial omics data [14].

404

405 In our work, we have also demonstrated the utility of SpaSEG in detecting spatial
406 variable genes based on our clustering result. For fair and comprehensive comparison,
407 we analyze two separate SVG detection methods: SpaGCN [16] and SpatialDE [45].
408 The former one takes spatial information into consideration when identifying SVGs,
409 while the other one detects SVGs without the guidance of spatial domains. SpaSEG

410 identified 490 SVGs compared to SpaGCN (458 SVGs) in total in sample 151673.
411 More specifically, there are about half of the SVGs enriched in white matter that are
412 only detected by our methods while SpaGCN not, although both methods have many
413 overlapping SVGs. Besides, there are more than 4000 SVGs identified by SpatialDE.
414 However, many of them failed to exhibit spatial patterns. Thus, SpaSEG could serve as
415 a potential tool for researchers to discover novel marker genes. In addition, our research
416 has also shown the ability of SpaSEG in dissecting the spatial cell-cell interaction in
417 adult mouse brain and IDC. The clustering results of SpaSEG in IDC and MB are
418 concordant with the manual annotation from pathologist and the reference panel from
419 Allen Mouse Brain Atlas respectively. More concretely, the heatmap of L-R pairs
420 indicates that the most active regions in mouse brain are cerebral cortexes and
421 hippocampus, which corresponds to previous studies [46]. Moreover, SpaSEG could
422 spatially visualize the distribution of immune cell in IDC through deconvolution and
423 further research could be undertaken to study the tumor microenvironment between the
424 tumor cells and macrophage, T cells and B cells, etc in molecular level through L-R
425 analysis.

426

427 Histology images are a new modality along with the ST data and the tissue
428 morphological features have a strong connection with the corresponding gene
429 expression around the specific spot [47, 48]. Recent studies such as SpaGCN and
430 stLearn have made efforts to incorporate histological images into their algorithms but
431 they are unable to achieve the finest clustering results, as demonstrated in our study.
432 One possible reason could be that there are no obvious morphological features among
433 the adjacent layers in DLPFC. Besides, the artifacts such as batch effects in the process

434 of Hematoxylin and Eosin (HE) staining and noise(quality) control of the H&E images
435 have a great influence on the final results. Our future research direction may lie in the
436 development of robust algorithms that seamlessly incorporate both modalities'
437 information together to achieve optimal performance. Another utility of H&E images
438 is resolution enhancement in ST data. While our work mainly focused on ST data from
439 10X genomics and Stereo-seq, the former one usually has lower resolution and
440 sensitivity, which limits their usefulness in studying detailed expression patterns and
441 uncovering comprehensive tissue anatomical structure. Recent works have
442 demonstrated the applicability of histological images in inferring accurate full-
443 transcriptome spatial gene expression at the same resolution as the image data (XFuse
444 [49]), which could be further used as a data enhancement approach for pre-processing
445 step of the low-resolution ST data. Further research could be undertaken to explore how
446 the imputed ST data would be used to train our algorithm and improve the clustering
447 accuracy.

448 In conclusion, this work presents SpaSEG, an efficient and scalable unsupervised deep
449 learning algorithm for ST data clustering. The results of our study also indicate the
450 applicability of our algorithm in various downstream analyses, such as SVGs
451 identification, cell-cell interaction and trajectory inference. Therefore, we believe that
452 SpaSEG could serve as a valuable tool to benefit ST data analysis in the future.

453 **Methods**

454 **Data preprocessing:**

455 SpaSEG takes transcriptome-wide gene expression profile with spatial coordinates as
456 inputs. Genes expressed in less than five spots or bins are excluded for all datasets. We

457 also eliminate poor spots with fewer than 200 expressed genes. The reserved raw gene
458 counts per spot are further normalized using the library size, and scaled by log-
459 transformation. Principal component analysis (PCA) is then performed on the gene
460 expression data in an $N \times M$ matrix with N spots and M genes, and top d PCs per
461 spot were subsequently extracted. The optimal value $d \in \{15, 50, 100\}$, varies from 15
462 to 100, depending on different sequencing platforms (Supplementary Table 9). These
463 PCs are able to explain the sufficient variability in the data and mitigate the
464 computational intension, as well as yield the best spatial clustering performance
465 (Supplementary Figure 1). We further perform z -score normalization such that each
466 PC has zero mean and unit variance.

467 **Conversion of spatial gene expression data into image-like tensor**

468 To enable SRT data analysis through SpaSEG, we convert the gene expression data with
469 spatial information into an image-like tensor. In this tensor, a spot n in the SRT array
470 at row i and column j was represented as a feature vector of $\mathbf{s}_{i,j}^n \in \mathbb{R}^d$, where d is
471 the number of extracted PCs. As a result, an d -channel image-like tensor $\mathbf{X} =$
472 $\{\mathbf{s}_{i,j}^n\}_{n=1}^N \in \mathbb{R}^{H \times W \times d}$ is created, where N is the number of spots, H and W are the
473 height and width of the SRT array, $i \in \{1, 2, \dots, H\}$, $j \in \{1, 2, \dots, W\}$. For
474 simplification, we denote the image-like tensor by $\mathbf{X} = \{\mathbf{s}_n\}_{n=1}^N$ unless otherwise
475 specification.

476 **SpaSEG model development**

477 *SpaSEG architecture.* Relying on convolutional neural network (CNN) architecture, our
478 model starts with a batch normalization layer, followed by two convolutional blocks
479 and a refinement module consecutively (Fig. 1b). Each convolutional block is

480 composed of a 3×3 (kernel size) convolutional layer, a batch normalization layer,
481 and a leaky ReLU activation layer (intermediate parameter $\alpha = 0.2$). The two
482 convolution modules have u and v output channels, respectively. Finally, the
483 refinement module consists of only a 1×1 convolutional layer and a batch
484 normalization layer, yielding k output channels. It should be noted that the output size
485 of each convolutional layer in SpaSEG is maintained the same as input. For
486 simplification, we set u , v and k be equal to d in all experiments.

487 Formally, given the SRT data of a tissue slice that was represented by an image-like
488 tensor $\mathbf{X} = \{\mathbf{s}_n\}_{n=1}^N$, the feature representation of spot n can be learned by

$$489 \quad \mathbf{y}_n = f_{\Theta}(\mathbf{s}_n) \quad (1)$$

490 where $f_{\Theta}(\cdot)$ is the SpaSEG network with the trainable parameter Θ that can be
491 updated during an iterative training process, $\mathbf{y}_n = [y_n^1, y_n^2, \dots, y_n^k] \in \mathbb{R}^k$. Then, the
492 pseudo-label for spot n can be given by

$$493 \quad c_n = \underset{t}{\operatorname{argmax}} y_n^t, \quad t = 1, 2, \dots, k \quad (2)$$

494 *Loss Function.* We treat the spatial domain identification as spot-wise classification
495 problem, where the class label of each spot can be viewed as a segment. To train
496 SpaSEG, we first consider the most commonly used cross entropy loss with L2-
497 norm regularization over pseudo-label as follows.

$$498 \quad \mathcal{L}_{\text{seg}} = -\sum_{n=1}^N \sum_{t=1}^k \mathbb{I}(c_n = t) \log(p_n^t) + \lambda \|\Theta\|_2^2 \quad (3)$$

499 where $\mathbb{I}(x) = \begin{cases} 1, & \text{if } x \text{ is true} \\ 0, & \text{otherwise} \end{cases}$, $p_n^t = e^{y_n^t} / \sum_{t=1}^k e^{y_n^t}$, and λ is regularization
500 parameter that controls the L2-norm regularization penalty and we set it to 0.00001

501 in our experiments.

502 To encourage the class label to be the same as those of spatially adjacent spots, we
503 follow the previous work [23] to introduce a spatial-smoothness loss function that
504 considers the horizontal and vertical differences of feature representations, which
505 is defined as

$$506 \quad \mathcal{L}_{\text{spa}} = \sum_{i=1}^{W-1} \sum_{j=1}^{H-1} \|\mathbf{y}_{i+1,j} - \mathbf{y}_{i,j}\|_1 + \|\mathbf{y}_{i,j+1} - \mathbf{y}_{i,j}\|_1$$

507 Consequently, the overall loss is then given by

$$508 \quad \mathcal{L}_{\text{overall}} = \alpha \mathcal{L}_{\text{seg}} + \beta \mathcal{L}_{\text{spa}}$$

509 where α and β are weighting factors for segmentation and spatial smoothness,
510 which are set to be 0.4 and 0.7, respectively.

511 SpaSEG training

512 Rather than randomly initializing parameters of SpaSEG that usually yields unstable
513 results, we pre-train SpaSEG using MSE loss defined as $\mathcal{L}_{\text{pre}} = \frac{1}{N} \sum_{n=1}^N \|\mathbf{s}_n - \mathbf{y}_n\|_2^2$
514 during the first 400 training epochs to initialize the model parameters. this iterative
515 process could stabilize the model performance and reinforce the entire algorithm to
516 update the model in a desirable direction. In the subsequent epochs, feature
517 representation \mathbf{y}_n and the corresponding pseudo-label c_n for each spot was obtained.
518 SpaSEG then calculates and backpropagates the overall loss $\mathcal{L}_{\text{overall}}$ to update the
519 model parameters. This process is repeated until either the number of iterations exceeds
520 the pre-defined maximum, or a minimum number of unique class labels is attained.

521 Otherwise, if the model failed to achieve the minimum number of class labels, an
522 optional refinement process is proposed to enhance the final segmentation result from
523 SpaSEG. In this process, the mean of the image-like tensor $\{\mathbf{s}_n^k\}_{n=1}^N$ for each cluster
524 along the d -channel are calculated, where k is the cluster label assigned by SpaSEG.
525 Then the pairwise Euclidian distances are calculated between the clusters, denoted as
526 $D_{i,j}$ and i, j is the cluster labels. While the candidate spots that are spatially
527 separable among the clusters will be relabeled according to the smallest $D_{i,j}$. We
528 employed Adam optimizer with the default parameters $\beta_1 = 0.9$ and $\beta_2 = 0.999$ as
529 optimization method for the backpropagation. The learning rate was set to 0.002 and
530 the total number of epochs were set to 2100. Those optimal values for the hyper-
531 parameters of SpaSEG were determined via a combination of grid search and manual
532 tuning such that the best performance can be achieved.

533 **Spatial variable gene detection**

534 In order to identify spatially variable genes (SVGs) that have high expression in each
535 spatial cluster, we combined the cluster results with pre-processing datasets. For each
536 cluster, Scanpy implementation of the Wilcoxon rank-sum test was used to identify
537 SVGs (adjusted p value < 0.05). To further confirm that the SVGs have abundant
538 expression, we added three conditions, this refers to SpaGCN's method of identifying
539 SVG:

- 540 1) In the target cluster, count the ratio of gene expression spots to total spot;
- 541 2) For outside the target cluster, the percentage of spots expressing genes within the
542 target cluster and outside the clusters;
- 543 3) Expression fold change in target cluster and outside clusters.

544 And then we drew the spatial pattern map of each SVG expression on the tissue, which
545 are identified that SVGs are truly enriched in target cluster.

546 And further discovering the functions with SVGs, we did GO and Kyoto Encyclopedia
547 of Genes and Genomes (KEGG) pathways enrichment analysis of SVGs by
548 clusterProfiler package in R software.

549

550 **Cell type deconvolution**

551 Each spatial spot was annotated to a specific cell type deconvoluted from spatial data
552 and corresponding single cell reference datasets. The deconvolution of cell types was
553 implemented using cell2location [50], which is a Bayesian model for spatial mapping
554 of cell types. Given the complementary information from spatial resolved
555 transcriptomic data and single-cell RNA sequence, we applied this Bayesian model to
556 infer different cell types in different spatial locations. The training hyperparameters
557 defined manually are selected depending on the cell number of a spot and RNA
558 detection sensitivity. The cell type corresponding to the maximum score of each spot is
559 regarded as the cell type of the spot in this research.

560

561 **Ligand-receptor interaction**

562 The cellular interactions mediated by protein-protein interactions are significant for
563 understanding tissue structures and functions. Firstly, we randomly permuted the
564 SpaSEG cluster labels of all spots to create a null distribution for each L-R pair in each

565 pairwise comparison between two clusters by using cellphoneDB. Then the significant
566 interacting pairs were used to analysis ligand-receptor interactions between the clusters.

567 With the prior of significant L-R pairs, we calculated the expression of spatially co-
568 expressed L-R pairs using:

$$569 \quad e_{i,j}^{L_k-R_k} = \sqrt{\mathbf{x}_i^{L_k} \cdot \mathbf{x}_j^{R_k}}$$
$$570 \quad E_{L_k-R_k} = \sum_{i=1}^n \sqrt{\mathbf{x}_n^{L_k} \cdot \mathbf{x}_n^{R_k}}$$

571 where \mathbf{x}_i and \mathbf{x}_j represents the gene expression vector of spot i and spot j ,
572 respectively. $E_{i,j}$ represents the value of L-R pair in all spots. If one of the ligands and
573 receptors in a spot is zero (not expressed), the co-expression value of the spot is zero.
574 By calculating the geometric mean of gene expression values, we know that the
575 geometric mean of each receptor ligand is large when the expression of each receptor
576 ligand is similar, and the geometric mean is small when the expression difference is
577 large. We calculated Spearman correlations between cell-type score and L-R score,
578 which represents the corresponding L-R pairs expression in related cell type.

579 **Data description**

580 We applied SpaSEG to ST datasets with different resolutions generated by various
581 platforms, such as 10X genomics, Stereo-Seq, MERFISH, SeqFISH, Slide-SeqV2. The
582 DLPFC dataset generated by Visium platform contains 12 slice and each consists of
583 around 4000 spots [12]. These 12 sections are all manually annotated and are used to
584 benchmark our algorithm. For the Stereo-seq data, we artificially divided the expression

585 matrix into non-overlapping bins covering an area of $X \times X$ DNB, with
586 $X \in (20, 50, 100, 200)$ and the transcripts of the same gene are aggregated within each
587 bin. Specifically, the raw matrix of adult mouse coronal brain sample [8] contains
588 27,279 genes, which was divided into bin20(526,716 spots with 10 μm diameter),
589 bin50(84,724 spots with 25 μm diameter), bin100(21,368 spots with 50 μm diameter)
590 and bin200(5,420 spots with 100 μm diameter). The MERFISH sample (animal id =
591 1, Bregma = -0.24) was collected from a female mouse with no treatment performed in
592 the hypothalamic preoptic region [51], this sample data contains 6412 spots and
593 measured 161 genes expression values. The mouse hippocampus data from Slide-
594 seqV2[6] (id: Puck_200115_08) consists of 53208 spots and measured 23264 genes.
595 The sagittal sections of the seqFISH[27] sample was collected from 8-12 somite-stage
596 embryos (Embryonic days (E)8.5-E8.75) and contains 19416 locations and 351
597 barcoded genes are measured. The mouse embryo dataset [8] with 76453 spots and
598 27009 genes collected from E15.5 embryos that was from pregnant C57BL/6J female
599 mice, produced by Stereo-seq have been deposited to CNGB Nucleotide Sequence
600 Archive. We aggregated the raw bin 1 matrix into the final bin 50 matrix and assigned
601 coordinates for each bin. The IDC (invasive ductal carcinoma) [15] data was
602 downloaded from 10X Genomics, which was stained for nuclei with DAPI and anti-
603 CD3. There are totally 4,727 spots detected under tissue. The mean reads per spot is
604 40,795. The median genes per spots is 2,964. The IDC sample approximately include a
605 median of 21 cells per spot.

606

607 **Data availability**

608 The DLPFC dataset is publicly available at <http://research.libd.org/spatialLIBD/>. The
609 MERFISH sample data could be downloaded from
610 <https://datadryad.org/stash/dataset/doi:10.5061/dryad.8t8s248>. The Slide-seqV2 data
611 could be accessible at [Single Cell Portal \(broadinstitute.org\)](https://singlecell.broadinstitute.org/). The seqFISH data can be
612 downloaded from <https://content.cruk.cam.ac.uk/jmlab/SpatialMouseAtlas2020/>. The
613 IDC data is publicly available at
614 [https://www.10xgenomics.com/resources/datasets/invasive-ductal-carcinoma-stained-
615 with-fluorescent-cd-3-antibody-1-standard-1-2-0](https://www.10xgenomics.com/resources/datasets/invasive-ductal-carcinoma-stained-with-fluorescent-cd-3-antibody-1-standard-1-2-0). The mouse embryo bin50 could be
616 down form <https://db.cngb.org/search/project/CNP0001543> .

617

618 **Comparison with state-of-arts methods and evaluation.**

619 To demonstrate the superior performance in spatial transcriptomics data clustering, we
620 chose a commonly used non-spatial clustering method Leiden plus five recently
621 published state-of-the-art methods, including stLearn, Giotto, SpaGCN, BayesSpace,
622 and SEDR (Supplementary Table 2). To evaluate the effectiveness of SpaSEG in
623 integrating multiple tissue sections, two commonly used algorithms in scRNA-seq data
624 batch correction, Harmony and LIGER are utilized to compare with SpaSEG.

625 *Leiden*. Leiden is a popular tool for single cell transcriptomics data clustering integrated
626 in Scanpy. The data preprocessing step is the same as SpaSEG and we ran *sc.tl.leiden*
627 in Scanpy and tune the resolution parameter to give us desirable number of clusters.

628 *stLearn*. *stLearn* is the first algorithm simultaneously integrating H&E information and
629 spatial transcriptomics data and allows various downstream analysis like cell-cell
630 interaction and trajectory inference. We ran the data processing with filtering gene at
631 least expressing in 1 cell and setting the number of principal components to 15, then
632 we follow the clustering pipeline of *stLearn*(version: 0.3.2) with the guidance of official
633 tutorial <https://stlearn.readthedocs.io/en/latest/>.

634 *Giotto*. *Giotto* is a toolbox for spatial data integrative analysis by utilizing hidden
635 Markov random field (HMRF) model. We follow the online tutorial of *Giotto*(version:
636 1.0.4): https://github.com/RubD/Giotto_site and set the *expression_threshold*
637 parameter to 1 in *filterGiotto* function and set *hvg = 'yes'*, *perc_cells > 3*,
638 *mean_expr_det > 0.4* in *gene_metadata* function when preparing data for dimensional
639 reduction. The spatial neighborhood network is created with the default parameters and
640 the number of ground truth clusters is employed for HMRF model clustering.

641 *SEDR*. *SEDR* uses a deep autoencoder to construct latent gene representation and a
642 variational graph autoencoder to embed spatial information. We ran *SEDR* code
643 indicated on the github repository: <https://github.com/JinmiaoChenLab/SEDR> with
644 default parameter settings.

645 *SpaGCN*. *SpaGCN* utilizes a graph convolutional network that combines gene
646 expression, spatial location and histology in spatial transcriptomics data analysis. We
647 follow the official tutorial of *SpaGCN*: <https://github.com/jianhuupenn/SpaGCN>
648 (version: 1.2.0) and set the *min_cell* to 3 when filtering genes, *alpha* to 1, *beta* to 49

649 when calculating adjacent matrix with histology image available. The learning rate and
650 max training epoch were set to 0.05 and 200, respectively.

651 *BayesSpace*. BayesSpace performs spatial clustering by introducing a spatial prior and
652 encouraging neighboring spots to belong to the same cluster. We ran BayesSpace
653 (version:1.2.1) followed by <https://github.com/edward130603/BayesSpace>. Top 200
654 highly variable genes are selected to perform PCA and we set q to the number of PCA
655 and d to the desirable cluster number, nrep to 50000 and gamma to 3, respectively.

656 Reference

657

- 658 1. Sonawane, A.R., et al., *Understanding Tissue-Specific Gene Regulation*. Cell
659 Rep, 2017. **21**(4): p. 1077-1088.
- 660 2. Lee, J.H., *Quantitative approaches for investigating the spatial context of gene*
661 *expression*. Wiley Interdiscip Rev Syst Biol Med, 2017. **9**(2).
- 662 3. Armingol, E., et al., *Deciphering cell-cell interactions and communication from*
663 *gene expression*. Nat Rev Genet, 2021. **22**(2): p. 71-88.
- 664 4. Moffitt, J.R., et al., *High-throughput single-cell gene-expression profiling with*
665 *multiplexed error-robust fluorescence in situ hybridization*. Proc Natl Acad Sci
666 U S A, 2016. **113**(39): p. 11046-51.
- 667 5. Lubeck, E., et al., *Single-cell in situ RNA profiling by sequential hybridization*.
668 Nat Methods, 2014. **11**(4): p. 360-1.
- 669 6. Stickels, R.R., et al., *Highly sensitive spatial transcriptomics at near-cellular*
670 *resolution with Slide-seqV2*. Nat Biotechnol, 2021. **39**(3): p. 313-319.
- 671 7. Stahl, P.L., et al., *Visualization and analysis of gene expression in tissue sections*
672 *by spatial transcriptomics*. Science, 2016. **353**(6294): p. 78-82.
- 673 8. Chen, A., et al., *Spatiotemporal transcriptomic atlas of mouse organogenesis*
674 *using DNA nanoball-patterned arrays*. Cell, 2022. **185**(10): p. 1777-1792 e21.
- 675 9. Marx, V., *Method of the Year: spatially resolved transcriptomics*. Nat Methods,
676 2021. **18**(1): p. 9-14.
- 677 10. Rao, A., et al., *Exploring tissue architecture using spatial transcriptomics*.
678 Nature, 2021. **596**(7871): p. 211-220.
- 679 11. Ji, A.L., et al., *Multimodal Analysis of Composition and Spatial Architecture in*
680 *Human Squamous Cell Carcinoma*. Cell, 2020. **182**(2): p. 497-514 e22.
- 681 12. Maynard, K.R., et al., *Transcriptome-scale spatial gene expression in the*
682 *human dorsolateral prefrontal cortex*. Nat Neurosci, 2021. **24**(3): p. 425-436.
- 683 13. Traag, V.A., L. Waltman, and N.J. van Eck, *From Louvain to Leiden:*
684 *guaranteeing well-connected communities*. Sci Rep, 2019. **9**(1): p. 5233.

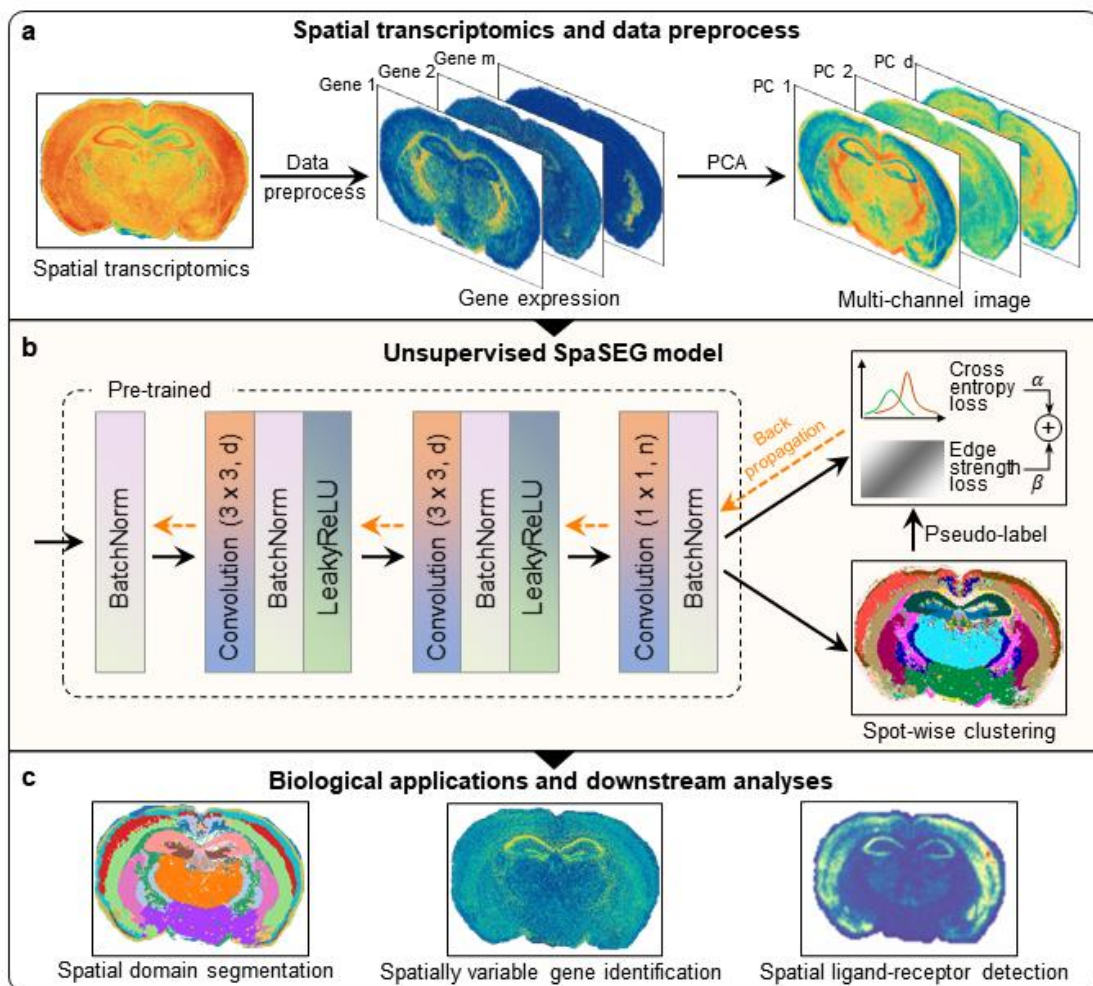
- 685 14. Fu, H., et al., 2021.
- 686 15. Zhao, E., et al., *Spatial transcriptomics at subspot resolution with BayesSpace*.
687 Nat Biotechnol, 2021. **39**(11): p. 1375-1384.
- 688 16. Hu, J., et al., *SpaGCN: Integrating gene expression, spatial location and*
689 *histology to identify spatial domains and spatially variable genes by graph*
690 *convolutional network*. Nat Methods, 2021. **18**(11): p. 1342-1351.
- 691 17. Pham, D., et al., 2020.
- 692 18. Dries, R., et al., *Giotto: a toolbox for integrative analysis and visualization of*
693 *spatial expression data*. Genome Biol, 2021. **22**(1): p. 78.
- 694 19. Edsgard, D., P. Johnsson, and R. Sandberg, *Identification of spatial expression*
695 *trends in single-cell gene expression data*. Nat Methods, 2018. **15**(5): p. 339-
696 342.
- 697 20. Svensson, V., S.A. Teichmann, and O. Stegle, *SpatialDE: identification of*
698 *spatially variable genes*. Nature Methods, 2018. **15**(5): p. 343-346.
- 699 21. Sun, S., J. Zhu, and X. Zhou, *Statistical analysis of spatial expression patterns*
700 *for spatially resolved transcriptomic studies*. Nature Methods, 2020. **17**(2): p.
701 193-200.
- 702 22. Walker, B.L., et al., *Deciphering tissue structure and function using spatial*
703 *transcriptomics*. Communications Biology, 2022. **5**(1).
- 704 23. Kim, W., A. Kanezaki, and M. Tanaka, *Unsupervised Learning of Image*
705 *Segmentation Based on Differentiable Feature Clustering*. IEEE Transactions
706 on Image Processing, 2020. **29**: p. 8055-8068.
- 707 24. Hubert, L. and P. Arabie, *Comparing partitions*. Journal of Classification, 1985.
708 **2**(1): p. 193-218.
- 709 25. Fowlkes, E.B. and C.L. Mallows, *A Method for Comparing Two Hierarchical*
710 *Clusterings*. Journal of the American Statistical Association, 1983. **78**(383): p.
711 553-569.
- 712 26. Sunkin, S.M., et al., *Allen Brain Atlas: an integrated spatio-temporal portal for*
713 *exploring the central nervous system*. Nucleic Acids Res, 2013. **41**(Database
714 issue): p. D996-D1008.
- 715 27. Lohoff, T., et al., *Integration of spatial and single-cell transcriptomic data*
716 *elucidates mouse organogenesis*. Nat Biotechnol, 2022. **40**(1): p. 74-85.
- 717 28. McCullough, K.M., et al., *Cell-type-specific interrogation of CeA Drd2 neurons*
718 *to identify targets for pharmacological modulation of fear extinction*. Transl
719 Psychiatry, 2018. **8**(1): p. 164.
- 720 29. Li, Z., et al., *The role of BDNF, NTRK2 gene and their interaction in*
721 *development of treatment-resistant depression: data from multicenter,*
722 *prospective, longitudinal clinic practice*. J Psychiatr Res, 2013. **47**(1): p. 8-14.
- 723 30. Wu, S.Z., et al., *A single-cell and spatially resolved atlas of human breast*
724 *cancers*. Nat Genet, 2021. **53**(9): p. 1334-1347.
- 725 31. Akatsu, C., et al., *The inhibitory coreceptor CD22 restores B cell signaling by*
726 *developmentally regulating Cd45(-/-) immunodeficient B cells*. Sci Signal, 2022.
727 **15**(723): p. eabf9570.
- 728 32. Coughlin, S., et al., *An extracatalytic function of CD45 in B cells is mediated by*

- 729 *CD22*. Proc Natl Acad Sci U S A, 2015. **112**(47): p. E6515-24.
- 730 33. Akatsu, C., et al., *The inhibitory coreceptor CD22 restores B cell signaling by*
731 *developmentally regulating Cd45 $-/-$ immunodeficient B cells*. Science
732 Signaling, 2022. **15**(723).
- 733 34. Broncy, L. and P. Paterlini-Bréchet, *Cancer-associated circulating atypical*
734 *cells with both epithelial and macrophage-specific markers*. Journal of
735 Laboratory and Precision Medicine, 2018. **3**: p. 91-91.
- 736 35. Schuette, V., et al., *Mannose receptor induces T-cell tolerance via inhibition of*
737 *CD45 and up-regulation of CTLA-4*. Proc Natl Acad Sci U S A, 2016. **113**(38):
738 p. 10649-54.
- 739 36. Holderried, T.A.W., et al., *Molecular and immune correlates of TIM-3*
740 *(HAVCR2) and galectin 9 (LGALS9) mRNA expression and DNA methylation*
741 *in melanoma*. Clin Epigenetics, 2019. **11**(1): p. 161.
- 742 37. Yang, R., et al., *Galectin-9 interacts with PD-1 and TIM-3 to regulate T cell*
743 *death and is a target for cancer immunotherapy*. Nat Commun, 2021. **12**(1): p.
744 832.
- 745 38. Yasinska, I.M., et al., *The Tim-3-Galectin-9 Pathway and Its Regulatory*
746 *Mechanisms in Human Breast Cancer*. Front Immunol, 2019. **10**: p. 1594.
- 747 39. Orimo, A., et al., *Stromal fibroblasts present in invasive human breast*
748 *carcinomas promote tumor growth and angiogenesis through elevated SDF-*
749 *1/CXCL12 secretion*. Cell, 2005. **121**(3): p. 335-48.
- 750 40. Zhu, G., et al., *CXCR3 as a molecular target in breast cancer metastasis:*
751 *inhibition of tumor cell migration and promotion of host anti-tumor immunity*.
752 Oncotarget, 2015. **6**(41): p. 43408-19.
- 753 41. Jackson, H.W., et al., *TIMPs: versatile extracellular regulators in cancer*. Nat
754 Rev Cancer, 2017. **17**(1): p. 38-53.
- 755 42. Shu, C., et al., *C3a-C3aR signaling promotes breast cancer lung metastasis via*
756 *modulating carcinoma associated fibroblasts*. J Exp Clin Cancer Res, 2020.
757 **39**(1): p. 11.
- 758 43. Ferrara, N., H.P. Gerber, and J. LeCouter, *The biology of VEGF and its receptors*.
759 Nat Med, 2003. **9**(6): p. 669-76.
- 760 44. Lein, E.S., et al., *Genome-wide atlas of gene expression in the adult mouse brain*.
761 Nature, 2007. **445**(7124): p. 168-76.
- 762 45. Svensson, V., S.A. Teichmann, and O. Stegle, *SpatialDE: identification of*
763 *spatially variable genes*. Nat Methods, 2018. **15**(5): p. 343-346.
- 764 46. Ero, C., et al., *A Cell Atlas for the Mouse Brain*. Front Neuroinform, 2018. **12**:
765 p. 84.
- 766 47. He, B., et al., *Integrating spatial gene expression and breast tumour*
767 *morphology via deep learning*. Nat Biomed Eng, 2020. **4**(8): p. 827-834.
- 768 48. Tan, X., et al., *SpaCell: integrating tissue morphology and spatial gene*
769 *expression to predict disease cells*. Bioinformatics, 2020. **36**(7): p. 2293-2294.
- 770 49. Bergenstrahle, L., et al., *Super-resolved spatial transcriptomics by deep data*
771 *fusion*. Nat Biotechnol, 2022. **40**(4): p. 476-479.
- 772 50. Kleshchevnikov, V., et al., *Cell2location maps fine-grained cell types in spatial*

773 *transcriptomics*. Nat Biotechnol, 2022. **40**(5): p. 661-671.
774 51. Moffitt, J.R., et al., *Molecular, spatial, and functional single-cell profiling of the*
775 *hypothalamic preoptic region*. Science, 2018. **362**(6416).
776

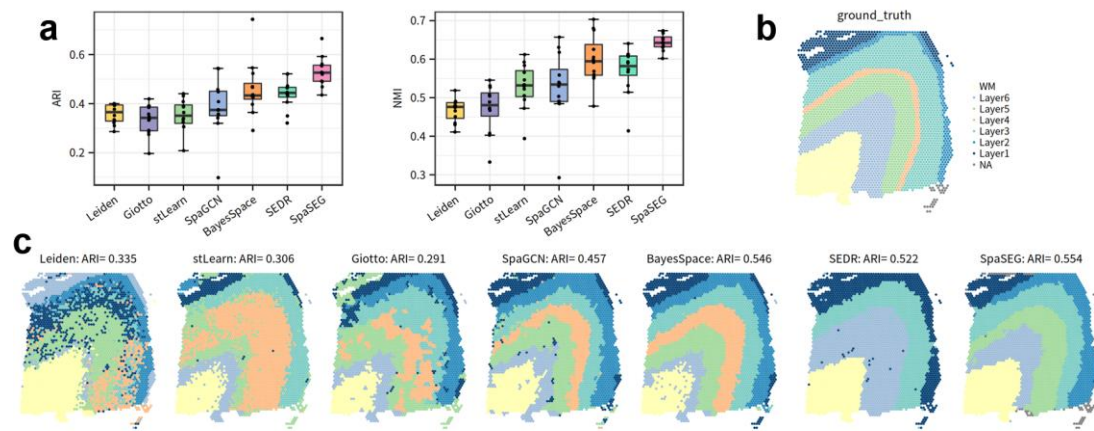
777 **Figure legend**

778 **Figure 1. Overview of SpaSEG.** **a.** Spatial transcriptomics data preprocessing and data
779 preparation step for SpaSEG. **b.** SpaSEG takes the image-like low dimensional feature
780 vector as input, then spot-wise labels are assigned through iterative unsupervised CNN
781 model training with gene similarity loss and spatial continuity loss. **c.** Biological
782 application and downstream analysis for SpaSEG, including spatial domain
783 identification, spatial variable detection, spatial ligand receptor detection.



784

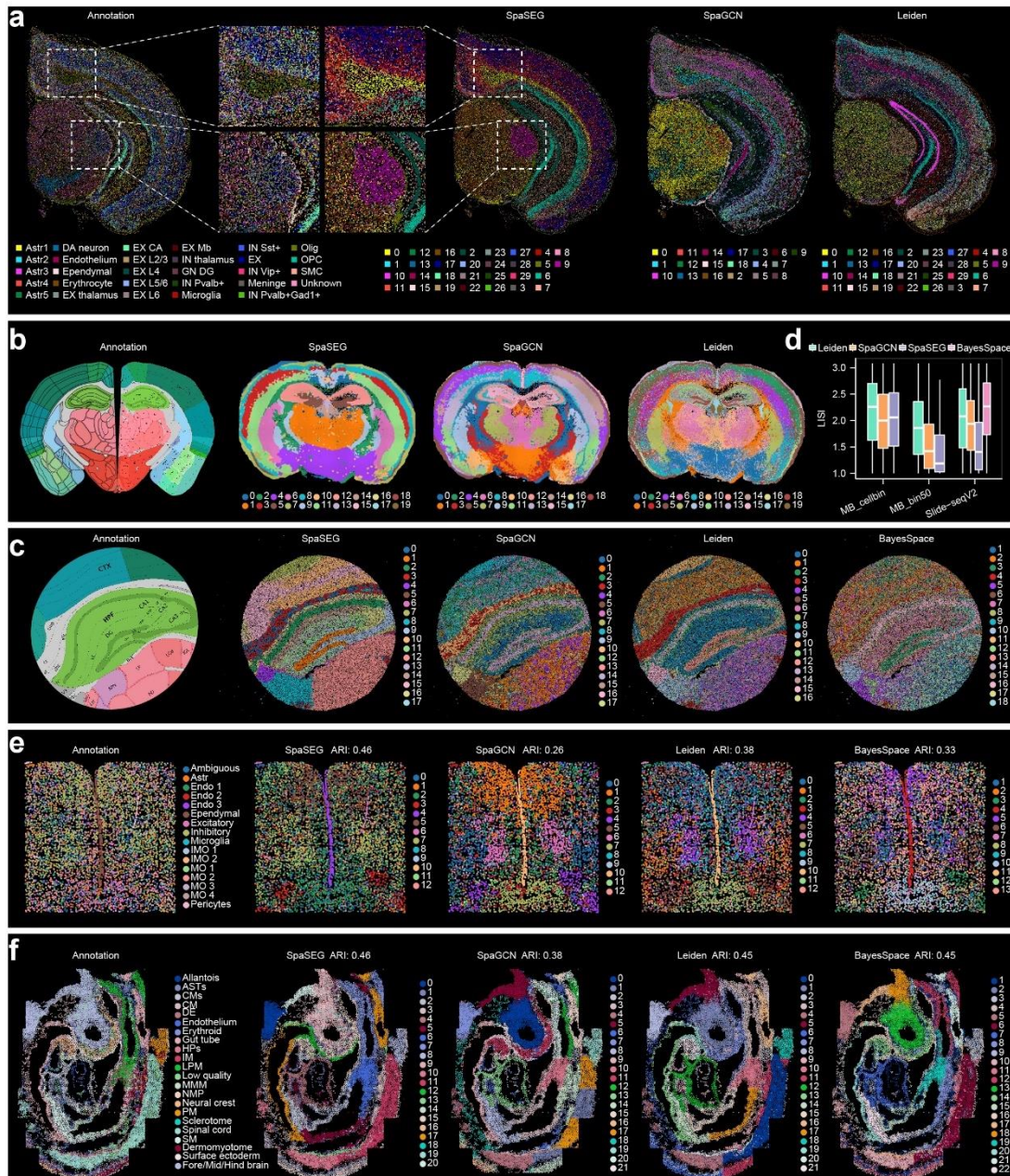
785 **Figure 2. Algorithms comparison in 10X DLPFC.** **a**, The average ARI, NMI score
786 among 12 DLPFC slices between SpaSEG and the other spatial methods. **b**, Annotated
787 ground truth for sample 151673. **c**, Spatial domain results for SpaSEG and other spatial
788 clustering methods in sample 151673.



789

790 **Figure 3. Robustness and scalability of SpaSEG in different spatial platforms.** **a**,
791 from left to right, the segmented Stereo-seq mouse brain cellbin annotation in the
792 original paper. The cell composition between the annotation and SpaSEG clusters in
793 two specific zoomed-in areas. SpaSEG cell segmentation results. SpaGCN clustering
794 results. Leiden clustering results. **b**, from left to right. Annotated mouse brain coronal
795 sections from Allen Brain Atlas. The clustering results of SpaSEG, SpaGCN and Leiden
796 respectively in Stereo-seq MB bin50 data. **c**, The LISI score calculated from SpaSEG,
797 SpaGCN and Leiden spatial clustering labels in MB cellbin, MB bin50 and Slideseq2
798 datasets. **d**, from left to right. The annotated structure of mouse hippocampus from
799 Allen Brain Atlas. Spatial domain results of SpaSEG, SpaGCN, Leiden and BayesSpace
800 in SlideseqV2. **e**, from left panel to right panel. The annotated celltype spatial
801 distribution of mouse hypothalamic preoptic region in the original paper. Spatial
802 clustering results of SpaSEG, SpaGCN, Leiden and BayesSpace in MERFISH dataset.
803 **f**. from left panel to right panel. The spatial map of cell composition during mouse
804 organogenesis in seqFISH data. Spatial clustering results of SpaSEG, SpaGCN, Leiden
805 and BayesSpace in the forementioned dataset. Astr: Astrocyte; Endo: Endothelial; IMO:

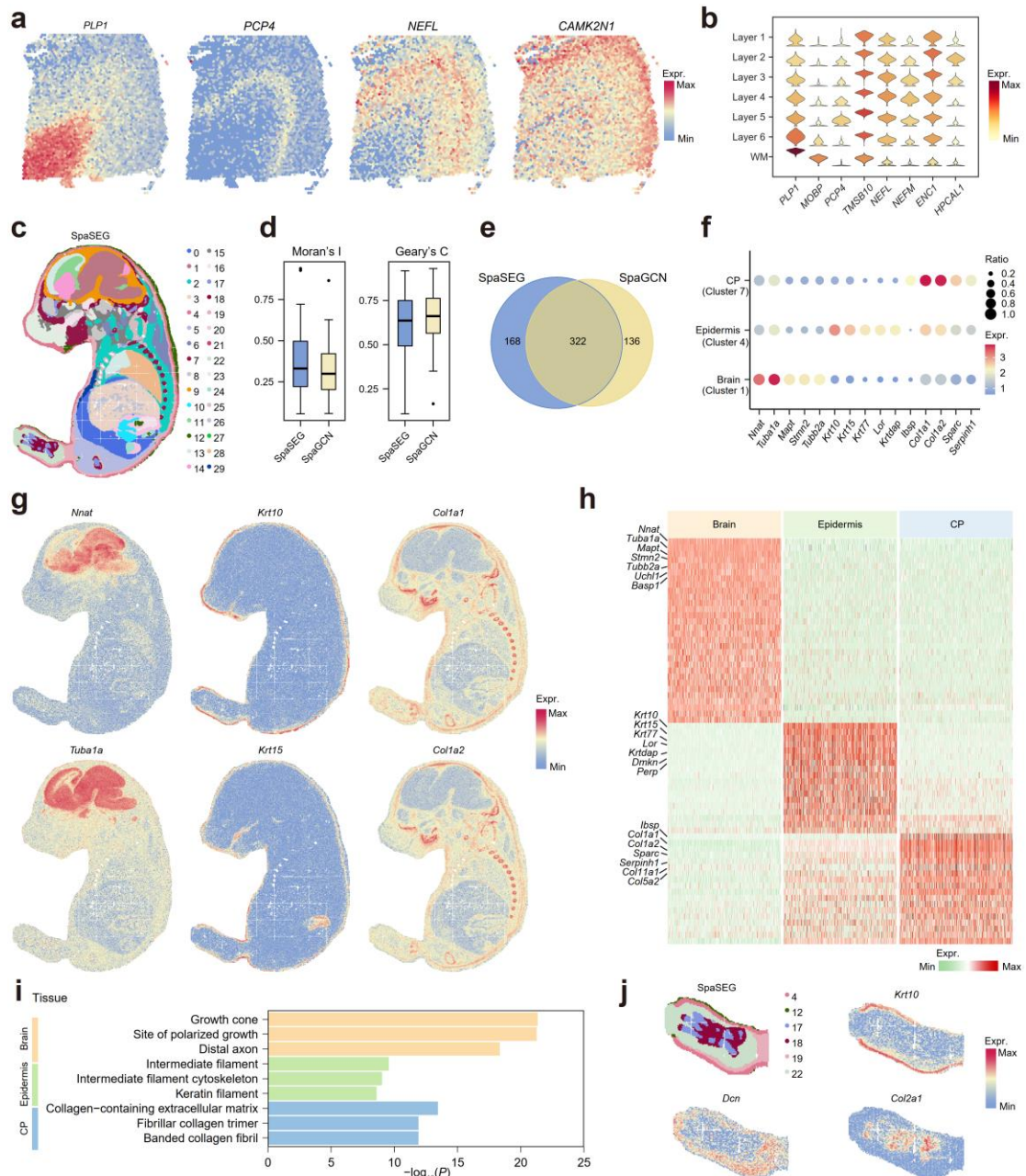
806 OD Immature; MO: OD Mature; ASTs: Anterior somitic tissues; CMs: Cardiomyocytes;
 807 CM: Cranial mesoderm; DE: Definitive endoderm; HPs: Haematoendothelial
 808 progenitors; IM: Intermediate mesoderm; LPM: Lateral plate mesoderm; MMM:
 809 Mixed mesenchymal mesoderm; PM: Presomitic mesoderm; SM: Splanchnic
 810 mesoderm.



811

812

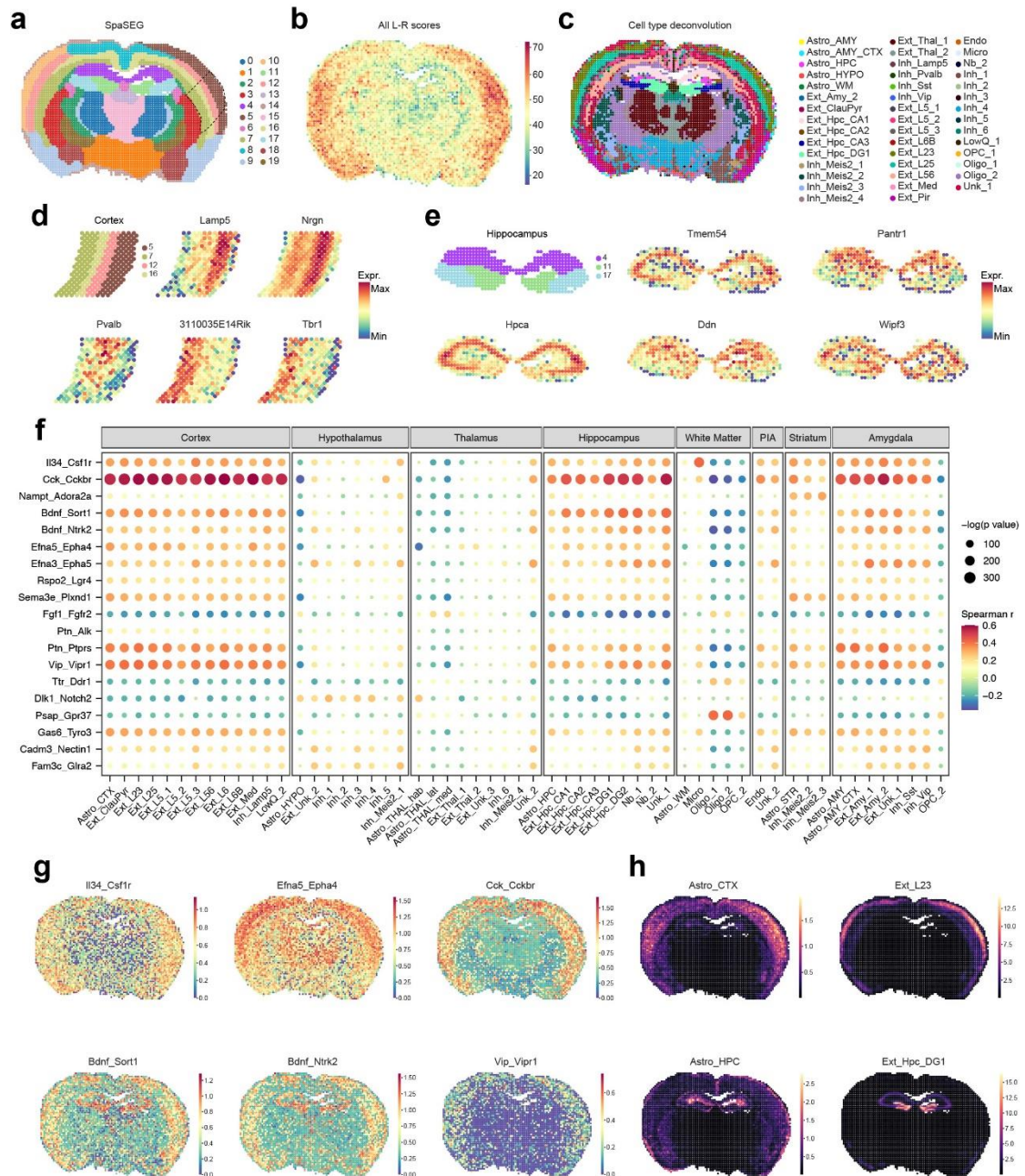
813 **Figure 4. Spatial clusters and SVGs detected in the DLPFC slices and Mouse**
814 **embryo. a**, Spatial expression pattern of the DLPFC's SVGs detected SpaSEG. **b**,
815 Bubble map of spatially differential genes obtained by SpaSEG in DLPFC (151673). **c**,
816 Spatial domain results for SpaSEG spatial clustering methods in mouse embryo. **d**,
817 Moran's I and Geary's C values for SVGs detected by SpaSEG(n=490) and SVGs
818 detected by SpaGCN (n=458). **e**, Venn diagram for SVGs detected by SpaSEG and
819 SpaGCN in the mouse embryo data. **f**, Violin plot of spatially differential genes
820 obtained by SpaSEG in mouse embryonic. **g**, spatial expression of mouse embryo's
821 brain, epidermis, cp. **h**, Spatial expression heatmap of the SVGs in the mouse embryo's
822 brain, epidermis and cp. **i**, GO pathway enrichment analysis of mouse embryo's brain,
823 epidermis, cp. **j**, spatially clusters of mouse toe and spatial expression of mouse toe.



824

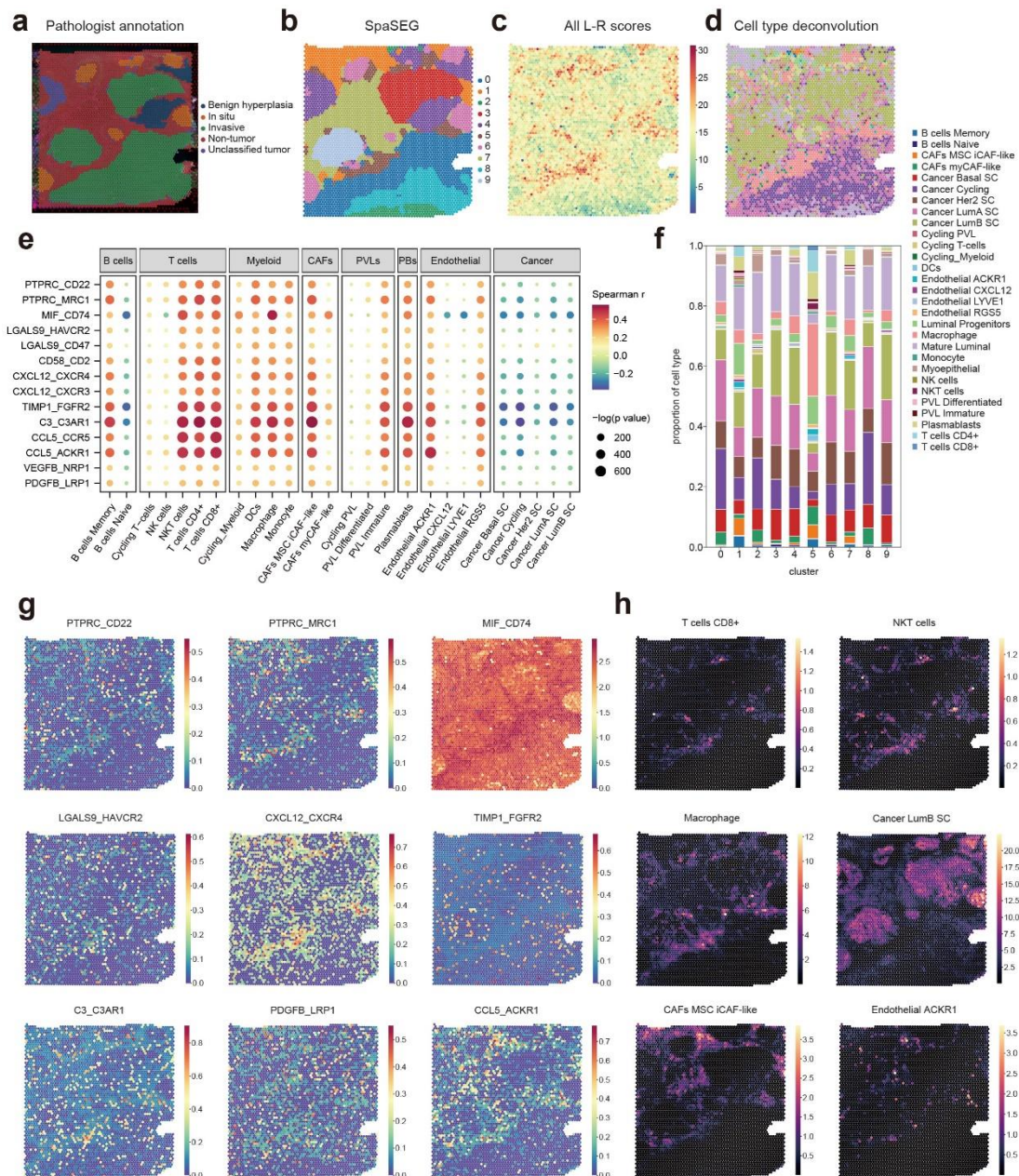
825 **Figure 5. Cell-cell interaction analysis of the adult mouse brain. a**, The workflow
 826 of cell-cell interaction. **b**, The result of SpaSEG clustering. **c**, Spatial expression of all
 827 significant L-R pairs. **d**, Spatially variable gene expression of zoomed-in cortex (cluster
 828 5, 7, 12, 16). The top5 SVGs and SpaSEG clustering for cortex are shown. **e**, Spatially
 829 variable gene expression of hippocampus (cluster 4, 7, 11) based on SpaSEG clustering.
 830 **f**, The Spearman correlation of cell type scores and L-R expression values. The

831 Spearman correlation values are represented by color. P values are represented by circle
 832 size. **g**, Significant L-R pairs of cortex area and hippocampus. **h**, A subset of cell types
 833 in the cortex and hippocampus, the proportions of which are estimated by cell2location.



834
 835 **Figure 6. Cell-cell interaction analysis of IDC. a**, The raw image of the IDC sample.
 836 **b**, The result of SpaSEG clustering. **c**, Spatial expression of all significant L-R pairs. **d**,
 837 The distribution of dominant cell types corresponding to the maximum score. **e**, The

838 Spearman correlation of cell type scores and L-R expression values. The Spearman
 839 correlation values are represented by color. P values are represented by circle size. **f**,
 840 Proportion of 29 cell types in each cluster. **g**. Significant L-R pairs of immune area and
 841 cancer area. **h**, Spatial distribution of a subset of immune cells (T cells CD8+, NKT
 842 cells, Macrophage and DCs) and stromal cells (CAFs MSC iCAF-like and Endothelial
 843 ACKR1).



844